

Hydrodynamic simulations of relativistic heavy-ion collisions with different calculations of the QCD equation of state

J. Scott Moreland¹ and Ron A. Soltz²

¹*Department of Physics, Duke University, Durham, NC 27708-0305*

²*Lawrence Livermore National Laboratory, Livermore, CA 94551-0808*

(Dated: September 1, 2015)

I. INTRODUCTION

Quantum Chromodynamics (QCD) predicts that at sufficiently high temperature or density, nuclear matter exists in a state of deconfined state of quarks and gluons known as a quark-gluon plasma (QGP). This state of matter filled the early universe several microseconds after the big bang and is now recreated and studied in the laboratory by colliding heavy ions at relativistic energies at the Relativistic Heavy Ion Collider (RHIC) and the Large Hadron Collider (LHC).

Quantitative model to data comparison, using simulations based on relativistic hydrodynamics, is the primary means to extract properties of QGP produced by relativistic heavy-ion collisions which expands and freezes into hadrons too quickly for direct observation. These hydrodynamic descriptions require two essential ingredients to specify the full time evolution of the QGP fireball: initial conditions which describe the thermal profile of the QGP droplet at some early starting time and a QCD Equation of State (EoS) which interrelates the energy density, pressure and temperature of each fluid cell in local thermal equilibrium.

Lattice discretization is the only reliable method to calculate the QCD equation of state in the vicinity of the QGP phase transition and hence constitutes a critical component of hydrodynamic simulations. While lattice techniques are rigorous in their treatment of the underlying QCD Lagrangian, they are subject to statistical and systematic errors inherent in the lattice discretization procedure. These errors are manifest in differences in the continuum extrapolated QCD trace anomaly and lead to an overall uncertainty in the true value of the QCD equation of state at zero baryochemical potential.

To date there have been few sensitivity studies on the influence of the EoS on hydrodynamic simulation results. They have been limited to studies of the order of the phase transition [1], different parameterization schemes for the LQCD EoS [2] and data driven Bayesian techniques to constrain parameterizations of the EoS motivated by LQCD calculations [3]. However, a sensitivity study on the inherent errors in the LQCD EoS has not yet been performed, primarily because continuum extrapolations for the LQCD EoS at zero baryon density have only recently become available [4, 5]. In this work, we quantify the effect of lattice errors on simulations of relativistic heavy-ion collisions by comparing simulation predictions obtained with QCD EoS calculations by the Wuppertal-

Budapest collaboration using the stout fermion action [4] and the HotQCD collaboration using the HISQ/tree action [5]. We also compare to the older s95p-v1 parameterization [2] constructed from calculations performed on coarser $(32^3 \times 8)$ lattices using p4 and asqtad actions without continuum extrapolation. The equations of state are analyzed using a modern event-by-event hybrid simulation which couples viscous hydrodynamics to a hadronic afterburner to calculate flows, spectra and Bertsch-Pratt radii and are compared to measurements at the Relativistic Heavy-Ion Collider (RHIC). We also perform a set of calculations in which the HISQ/tree continuum EoS is sampled from within the published error range.

II. EQUATIONS OF STATE

The Wuppertal-Budapest, HotQCD and s95p-v1 EoS parameterizations used in this work all employ staggered fermion actions with varying level improvements: additional terms added to remove lattice artifacts and improve simulation convergence. For example, both the stout and HISQ/tree actions used by the Wuppertal-Budapest and HotQCD calculations contain additional smearing of the gluon links relative to p4 and asqtad actions used to construct the s95p-v1 parameterization. Moreover, the Wuppertal-Budapest stout action omits second order corrections in the lattice spacing which are common to the other three.

The three analyses are further distinguished by the granularity of the lattices used in each calculation. The p4 and asqtad results used in the s95p-v1 parameterization are from $(32^3 \times 8)$ lattices, referred to by the number of temporal dimension, $N_\tau = 8$, while the HISQ/tree continuum extrapolation was calculated for $N_\tau = 8, 10$, and 12, and the stout results for lattices with $N_\tau = 6, 8, 10$ and 12. For a more detailed discussion of the EoS calculations and relative improvements of the staggered fermion actions see [6].

LQCD EoS calculations are obtained from the trace of the stress-energy tensor, equal to the difference between the energy density and three times the pressure. This quantity is typically referred to as the interaction measure or trace anomaly because it measures deviations from the conformal equation of state. Once scaled by powers of the temperature, the trace anomaly forms a

dimensionless measure

$$I \equiv \frac{\Theta^{\mu\mu}(T)}{T^4} = \frac{e - 3p}{T^4}, \quad (1)$$

where Θ is the stress-energy tensor, e is the local fluid energy density, p the pressure and T the temperature.

Lattice calculations typically extend down to temperatures of ~ 130 MeV, where small deviations with the Hadron Resonance Gas (HRG) EoS may begin to develop. This is evident in Fig. 1, which shows the trace anomaly of the HRG EoS alongside results from the HotQCD and Wuppertal-Budapest (WB) collaborations with HISQ/tree and stout actions respectively, as well as the older s95p-v1 parameterization obtained using p4 and asqad actions. Both the HISQ/tree and stout EoS results begin to pull away from the HRG EoS at temperatures above 130 MeV, while the s95p-v1 parameterization agrees with the HRG results up to a matching temperature of 183.8 MeV by construction.

Although both the Wuppertal-Budapest and HotQCD collaborations have provided parameterizations suitable for insertion into hydrodynamic codes, the matching temperature of 130 MeV falls below the 155–165 MeV temperature range where hybrid simulations typically switch from relativistic viscous hydrodynamics to a microscopic kinetic description such as UrQMD [7, 8]. We note also that recent estimates for the freeze-out temperature derived from combining lattice calculations and experimental data also fall within this range [9, 10]. To ensure a self consistent description of the collision dynamics where the simulation switches from hydrodynamics to microscopic transport, we modify each lattice EoS to match the HRG EoS at the desired hydro-to-micro switching temperature. We thus define a new piecewise interaction measure

$$I(T) = \begin{cases} I_{\text{hrg}}(T) & T \leq T_1, \\ I_{\text{blend}}(T) & T_1 < T < T_2, \\ I_{\text{lattice}}(T) & T \geq T_2, \end{cases} \quad (2)$$

where I_{hrg} and I_{lattice} are the HRG and LQCD trace anomalies pictured in Fig. 1, and I_{blend} is a function

$$I_{\text{blend}} = (1 - z) I_{\text{hrg}} + z I_{\text{lattice}}. \quad (3)$$

which smoothly connects between the two in the temperature interval $T_1 < T < T_2$. The interpolation parameter $z \in [0, 1]$ is constructed to match the first and second derivatives at the endpoints of the interpolation interval,

$$z = 6x^5 - 15x^4 + 10x^3 \quad (4)$$

$$\text{where } x = (T - T_1)/(T_2 - T_1). \quad (5)$$

We fix the boundaries of the blending region $T_1 = 155$ MeV and $T_2 = 180$ MeV to impose matching at the switching temperature $T_{\text{sw}} = 155$ MeV which coincides with the pseudo-critical phase transition temperatures of the HotQCD and Wuppertal-Budapest EoS.

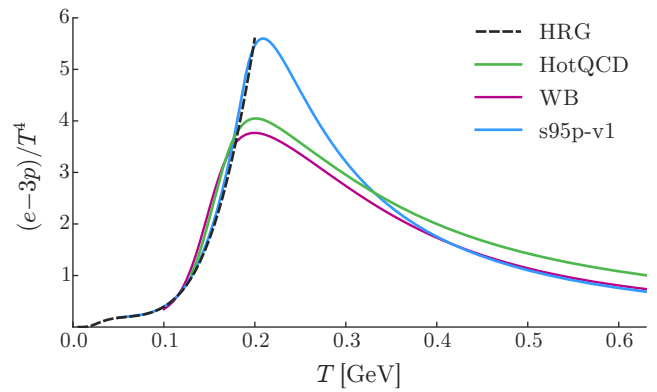


FIG. 1. The temperature scaled QCD interaction measure for the HRG, HotQCD, WB and s95p-v1 EoS as a function of temperature [2, 4, 5].

The modified interaction measures, labeled with a dagger to distinguish them from the published values, are plotted in Fig. 2. We see that the interpolation procedure imposes the necessary matching condition on either side of the switching temperature (vertical gray line) with minimal disturbance to the peak of the LQCD trace anomaly at higher temperatures. In Fig. 3 we plot the squared speed of sound $c_s^2 = dp/de$ for each modified interaction measure. The speed of sound of the HotQCD[†] and WB[†] equations of state are in good agreement while the S95[†] parameterization remains softer in a wider interval about the QGP phase transition. We note that the speed of sound in the HotQCD[†] and WB[†] parameterizations is clearly affected by the parametric transition (3) in the vicinity of the switching temperature (vertical gray line), but that the imposed matching maintains continuity.

With the trace anomalies in hand, the energy density,

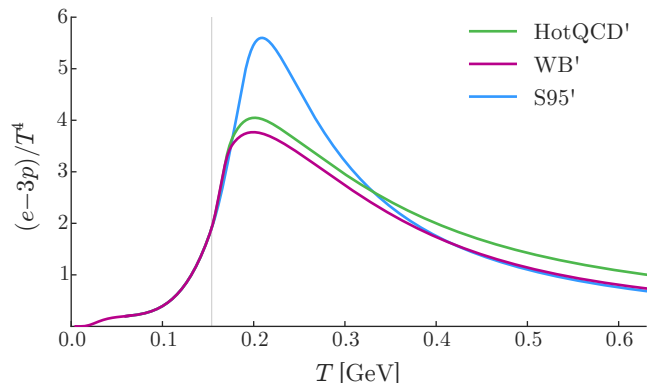


FIG. 2. The modified QCD interaction measure for the HotQCD[†], WB[†] and S95[†] EoS obtained from equation (2) and the corresponding lattice parameterizations in Fig. 1. The vertical gray line marks the hydro-to-micro switching temperature $T_{\text{sw}} = 155$ MeV.

pressure and entropy density are easily interrelated to specify the equation of state used in the analysis,

$$\frac{p(T)}{T^4} = \int_0^T dT' \frac{I(T')}{T'}, \quad (6)$$

$$\frac{e(T)}{T^4} = I(T) + 3 \frac{p(T)}{T^4}, \quad (7)$$

$$\frac{s(T)}{T^3} = \frac{e(T) + p(T)}{T^4}. \quad (8)$$

For clarity, Figs. 1–3 do not include the respective errors bands for the HotQCD and Wuppertal-Budapest trace anomalies, but both calculations devote considerable effort to providing an accurate error estimate for their respective calculations [4, 5]. Common contributions to the errors come from variations in spline fits to the interaction measures, differences between quadratic and quartic extrapolations in the lattice spacing, and small (2%) variations in the temperature scale. Errors are typical of order 5% for most quantities, and increase to 5–10% in the transition region where the curves are steepest.

III. HYBRID MODEL

The equations of state are embedded in the modern event-by-event VISHNU hybrid model which uses the VISH2+1 boost-invariant viscous hydrodynamics code to simulate the time evolution of the QGP medium and a microscopic UrQMD hadronic afterburner for subsequent evolution below the QGP transition temperature. Where necessary, free parameters of the model are tuned to facilitate model-to-data comparison with 200 GeV gold-gold collisions at RHIC. In this section, we briefly outline the implementation of the model used in the analysis; for a more detailed explanation of the VISHNU model, we refer the reader to [11].

A. Initial conditions

The hydrodynamic initial conditions are generated using a Monte Carlo Glauber model based on a common two-component ansatz which deposits entropy proportional to a linear combination of nucleon participants and binary nucleon-nucleon collisions,

$$dS/dy|_{y=0} \propto \frac{(1-\alpha)}{2} N_{\text{part}} + \alpha N_{\text{coll}} \quad (9)$$

where for the binary collision fraction, we use $\alpha = 0.14$ which has been shown to provide a good description of the centrality dependence of charged particle multiplicity in 200 GeV gold-gold collisions [12].

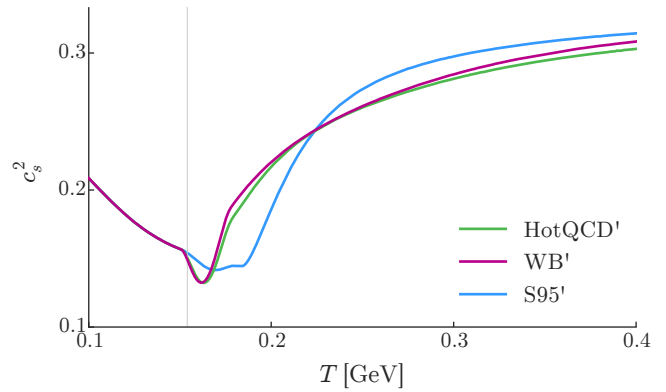


FIG. 3. Speed of sound squared c_s^2 plotted versus temperature T for the HotQCD[†], WB[†] and S95[†] equations of state used in this study. The vertical gray line indicates the switching temperature $T_{\text{sw}} = 155$ MeV where the model switches from fluid dynamics to a microscopic transport model.

The entropy is localized about each nucleon's transverse parton density $T_p(\mathbf{x})$,

$$dS/dy|_{y=0} \propto \sum_{i=0}^{N_{\text{part,A}}} w_i T_p(\mathbf{x} - \mathbf{x}_i) (1 - \alpha + \alpha N_{\text{coll},i}) + \sum_{j=0}^{N_{\text{part,B}}} w_j T_p(\mathbf{x} - \mathbf{x}_j) (1 - \alpha + \alpha N_{\text{coll},j}) \quad (10)$$

where the summations run over the participants in each nucleus, $N_{\text{coll},i}$ denotes the number of binary collisions suffered by the i -th nucleon and the proton density $T_p(\mathbf{x})$ is described by a Gaussian

$$T_p(\mathbf{x}) = \frac{1}{\sqrt{2\pi B}} \exp\left(-\frac{x^2 + y^2}{2B}\right) \quad (11)$$

with transverse area $B = 0.36 \text{ fm}^2$.

The random nucleon weights w_i in equation (10) are sampled independently from a Gamma distribution with unit mean

$$P_k(w) = \frac{k^k}{\Gamma(k)} w^{k-1} e^{-kw}, \quad (12)$$

and shape parameter $k = \text{Var}(P)^{-1}$ which modulates the variance of the distribution. Such fluctuations are typically added to reproduce the large multiplicity fluctuations observed in minimum bias proton-proton collisions [12–16]. In this work the shape parameter is fixed to $k = 1$ determined by a fit to the 200 GeV UA5 data [17].

The initial condition profiles, which provide the entropy density $dS/(d^2r_\perp d\eta \tau_{\text{therm}})$ at the QGP thermalization time, are finally rescaled by an overall normalization factor to fit the measured charged particle multiplicity in 0–10% centrality collisions.

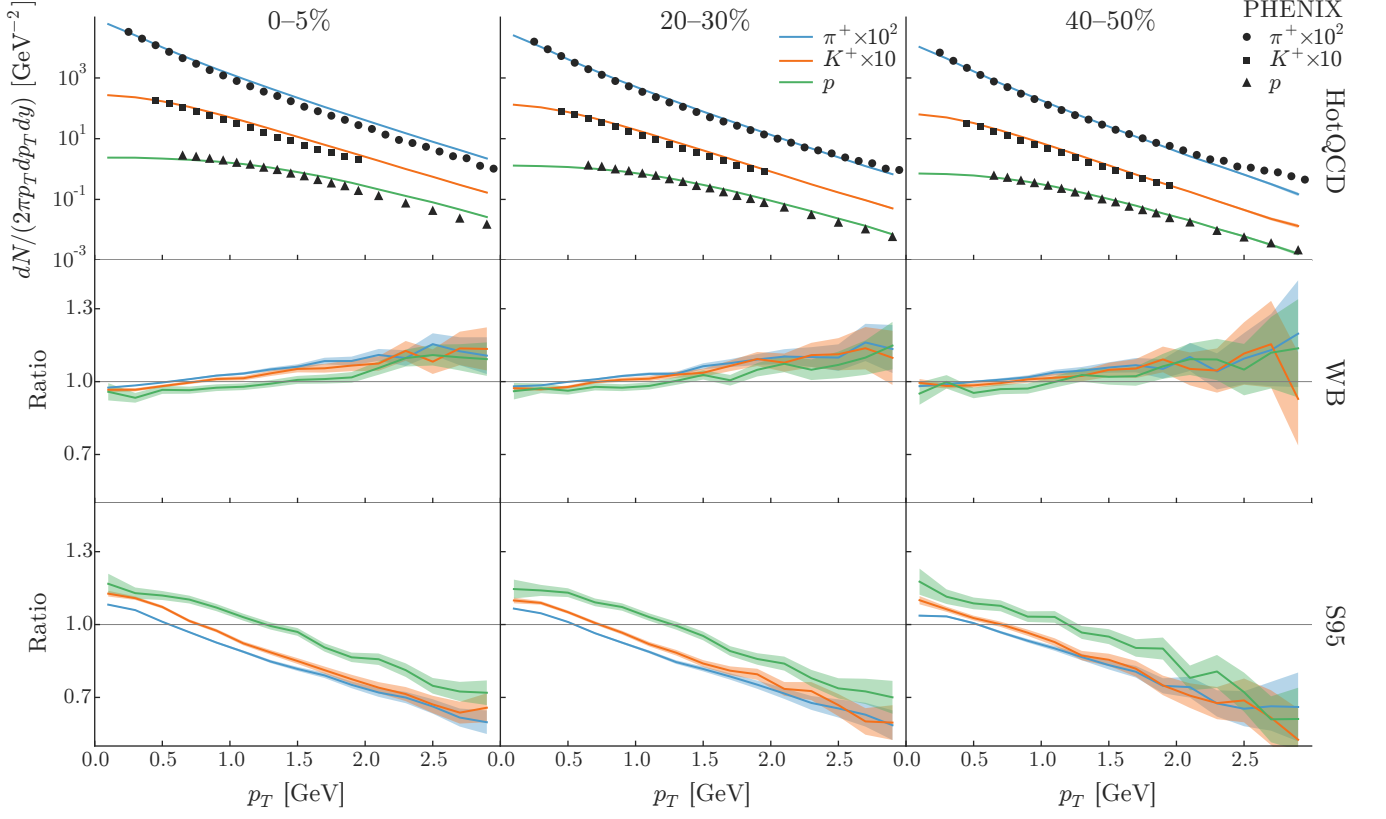


FIG. 4. Effect of the equation of state on transverse momentum spectra. Top row: model calculations using the HotQCD[†] equation of state plotted against PHENIX data for pions, kaons and protons (blue lines/circles, red lines/squares and green lines/triangles) in centrality bins 0–5%, 20–30% and 40–50% (columns left to right). Middle and bottom rows: ratios of the WB[†] and S95[†] invariant yields to the HotQCD[†] result. Shaded bands indicate two sigma statistical error.

B. Hydrodynamics and Boltzmann transport

The hydrodynamic equations of motion are obtained in VISHNew by solving the second-order Israel-Stewart equations,

$$\partial_\mu T^{\mu\nu} = 0, \quad T^{\mu\nu} = eu^\mu u^\nu - (p + \Pi)\Delta^{\mu\nu} + \pi^{\mu\nu}, \quad (13)$$

where the bulk pressure Π and shear stress $\pi^{\mu\nu}$ satisfy the relaxation equations,

$$\mathcal{D}\Pi = -\frac{1}{\tau_\Pi}(\Pi + \zeta\theta) - \frac{1}{2}\Pi\frac{\zeta T}{\tau_\Pi}d_\lambda\left(\frac{\tau_\Pi}{\zeta T}u^\lambda\right),$$

$$\Delta^{\mu\alpha}\Delta^{\nu\beta}\mathcal{D}\pi_{\alpha\beta} = -\frac{1}{\tau_\pi}(\pi^{\mu\nu} - 2\eta\sigma^{\mu\nu}) \quad (14)$$

$$-\frac{1}{2}\pi^{\mu\nu}\frac{\eta T}{\tau_\pi}d_\lambda\left(\frac{\tau_\pi}{\eta T}u^\lambda\right). \quad (15)$$

We follow the work in reference [12] and fix the bulk viscosity ζ and shear viscosity η in equation (14) using a constant specific shear viscosity $\eta/s = 0.08$ and vanishing bulk viscosity $\zeta/s = 0$ in the hydrodynamic phase of the simulation. It would be interesting to study the effect of bulk viscous corrections which are sensitive to the peak of

the QCD trace anomaly near the QGP phase transition [18]. Unfortunately, bulk viscous corrections do not have a straight forward implementation in the present hybrid model and are neglected in this work.

As previously explained in section II, the VISHNU hybrid model transitions from hydrodynamic field equations to microscopic transport at a sudden switching temperature T_{sw} at which the hydrodynamic energy-momentum tensor is particlized using the Cooper-Frye freezeout prescription,

$$E\frac{dN_i}{d^3p} = \int_\sigma f_i(x,p)p^\mu d^3\sigma_\mu \quad (16)$$

where f_i is the distribution function of particle species i , p^μ is its four-momentum and $d^3\sigma_\mu$ characterizes an element of the isothermal freezeout hypersurface defined by T_{sw} .

The sampled particles then enter the UrQMD simulation where the Boltzmann equation,

$$\frac{df_i(x,p)}{dt} = \mathcal{C}_i(x,p), \quad (17)$$

is solved to simulate all elastic and inelastic collisions between the particles with collision kernel \mathcal{C}_i until the system becomes too dilute to continue interacting. Finally,

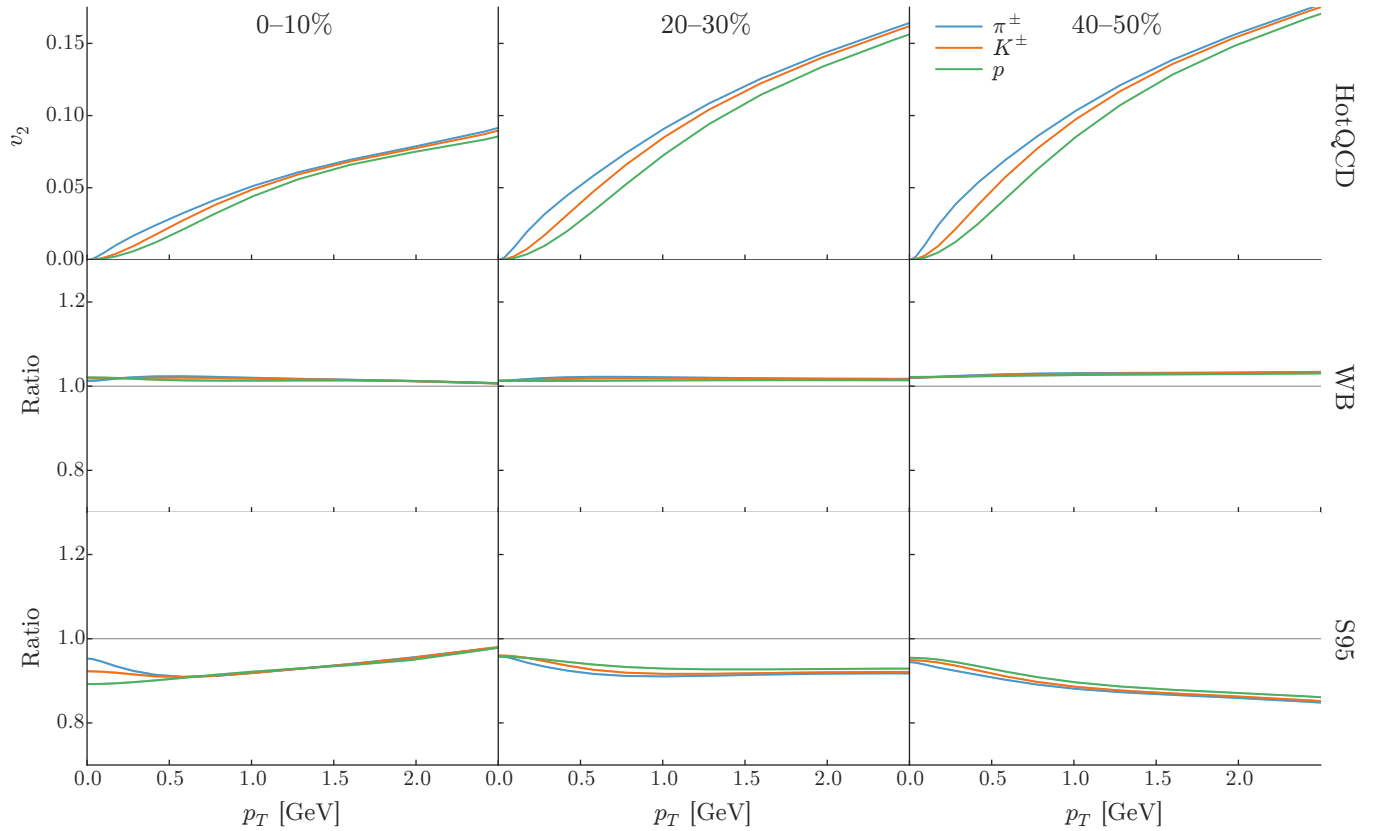


FIG. 5. Effect of the equation of state on differential elliptic flow $v_2(p_T)$ calculated from the Cooper-Frye freezeout hypersurface (19). Top row: model calculations using the HotQCD[†] equation of state for the elliptic flow $v_2(p_T)$ of pions, kaons and protons (blue, orange and green lines) in centrality bins 0–10%, 20–30% and 40–50% (columns left to right). Middle and bottom rows: ratios of the WB[†] and S95[†] elliptic flow to the HotQCD[†] result. Statistical errors are smaller than the linewidth and have been omitted.

the four-position, four-momentum and particle identification number of each particle recorded at the moment of last interaction.

IV. RESULTS

The results section is organized as follows. In sub-section IV A we calculate the particle spectra for each equation of state across three different centrality classes using the final particle information output by the hybrid simulation. In sub-section IV B we repeat the calculation for elliptic and triangular flow but perform the calculation on the hydrodynamic Cooper-Frye freezeout surface for reasons explained later in the text. In sub-section IV C we calculate the femtoscopic event-averaged Bertsch-Pratt radii, again using the final particle information output by the full hybrid calculation. Finally in sub-section IV D, we repeat the spectra and flow analysis using a sampling of equation of state curves from the HotQCD published errors.

All results presented in the following sections are based on 10^5 minimum bias events which are subdivided into

centrality classes according to initial entropy, e.g. the initial condition events with 20% highest entropy comprise centrality class 0–20%. Each hydrodynamic event is oversampled an additional four times to increase the number of particles in each event and suppress finite statistical error.

A. Particle spectra

Figure 4 shows the invariant yield $dN/(2\pi p_T dp_T dy)$ of positively charged pions, kaons and protons calculated from the hybrid model for the 0–5%, 20–30% and 40–50% centrality classes using the HotQCD[†], WB[†] and S95[†] equations of state constructed in section II.

The first row shows the HotQCD[†] yields obtained from the hybrid model plotted against observed pion, proton and kaon data from PHENIX. The second and third rows show the ratio of the invariant yields of the WB[†] and S95[†] equations of state over the the HotQCD[†] result. We see that the HotQCD[†] equation of state provides a good description of observed particle yields except for at moderate to large p_T in central collisions where the equa-

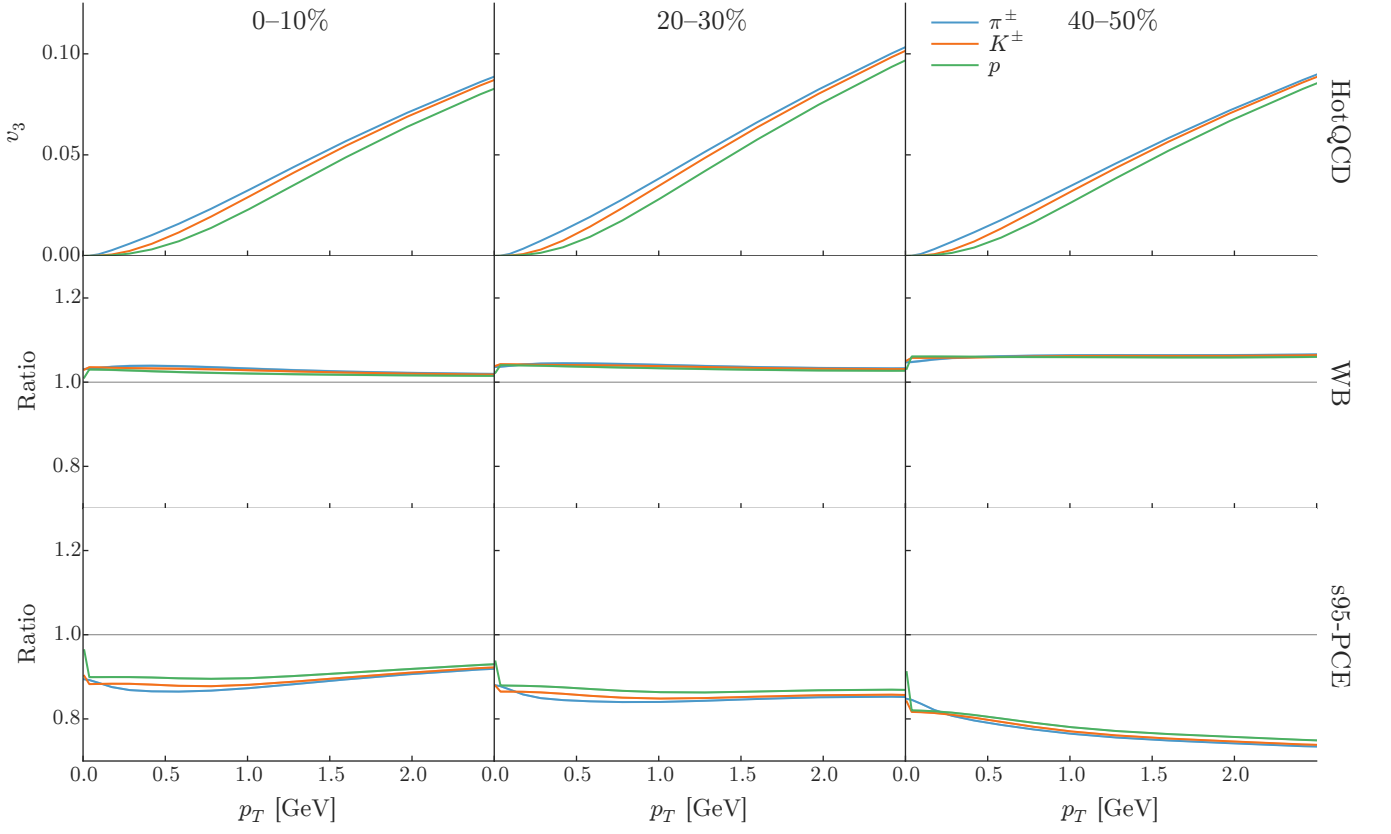


FIG. 6. Same as Fig. 5 but for differential triangular flow $v_3(p_T)$. Note that the y-axis limits in the top row are different.

tion of state overpredicts the data. This agreement would likely improve with more realistic initial conditions, bulk viscous corrections and/or more careful treatment of the hydro-to-micro switching temperature T_{sw} , and thus we defer from making any specific conclusions from the overall fit to data. It suffices to say that the most recent HotQCD lattice results provide a reasonable description of the PHENIX data and agrees within the overall uncertainty of the present model.

Looking at the second and third rows of the figure which show the ratios of the WB^\dagger and $S95^\dagger$ yields to the HotQCD † result, we see that the spectra predicted by the HotQCD † and WB^\dagger equations of state agree within statistical error, while the $S95^\dagger$ equation of state is appreciably softer and produces $\sim 10\%$ more particles at $p_T = 0.5$ GeV and $\sim 30\%$ fewer particles at $p_T = 2.5$ GeV across all three centralities.

B. Elliptic and triangular flows

The azimuthal anisotropy of final particle emission is characterized by the Fourier expansion

$$E \frac{d^3N}{d^3p} = \frac{1}{2\pi} \frac{d^2N}{dy p_T dp_T} \left(1 + \sum_{n=1}^{\infty} 2v_n \cos n(\phi - \Psi_{RP}) \right) \quad (18)$$

where ϕ is the direction of the emitted particle, Ψ_{RP} is the reaction plane angle of the event and v_n the anisotropic flow coefficient corresponding to the Fourier harmonic of order n .

The reaction plane angle cannot be measured experimentally and the anisotropic flow is typically estimated using multi-particle correlations such as two and four-particle cumulants. The statistical error of the event-averaged estimators is suppressed with both increasing event multiplicity and event sample size. This can pose a challenge for computationally intensive hybrid model calculations which typically cannot reach integrated luminosities comparable to experiment.

Statistical errors are particularly noxious in differential flow calculations at moderate to large p_T where particle statistics are limited. We circumvent this issue in the differential flow analysis and calculate the flow anisotropy of pions, kaons and protons directly from the Cooper-Frye freezeout surface using the built in routines in the VISHNU package according to

$$v_n(p_T) = \frac{\int d\phi_p e^{in\phi_p} dN/(dy p_T dp_T d\phi_p)}{\int d\phi_p dN/(dy p_T dp_T d\phi_p)}. \quad (19)$$

Consequently, the present flow sensitivity analysis does not include contributions from flow generated by the UrQMD hadronic afterburner which is identical for each

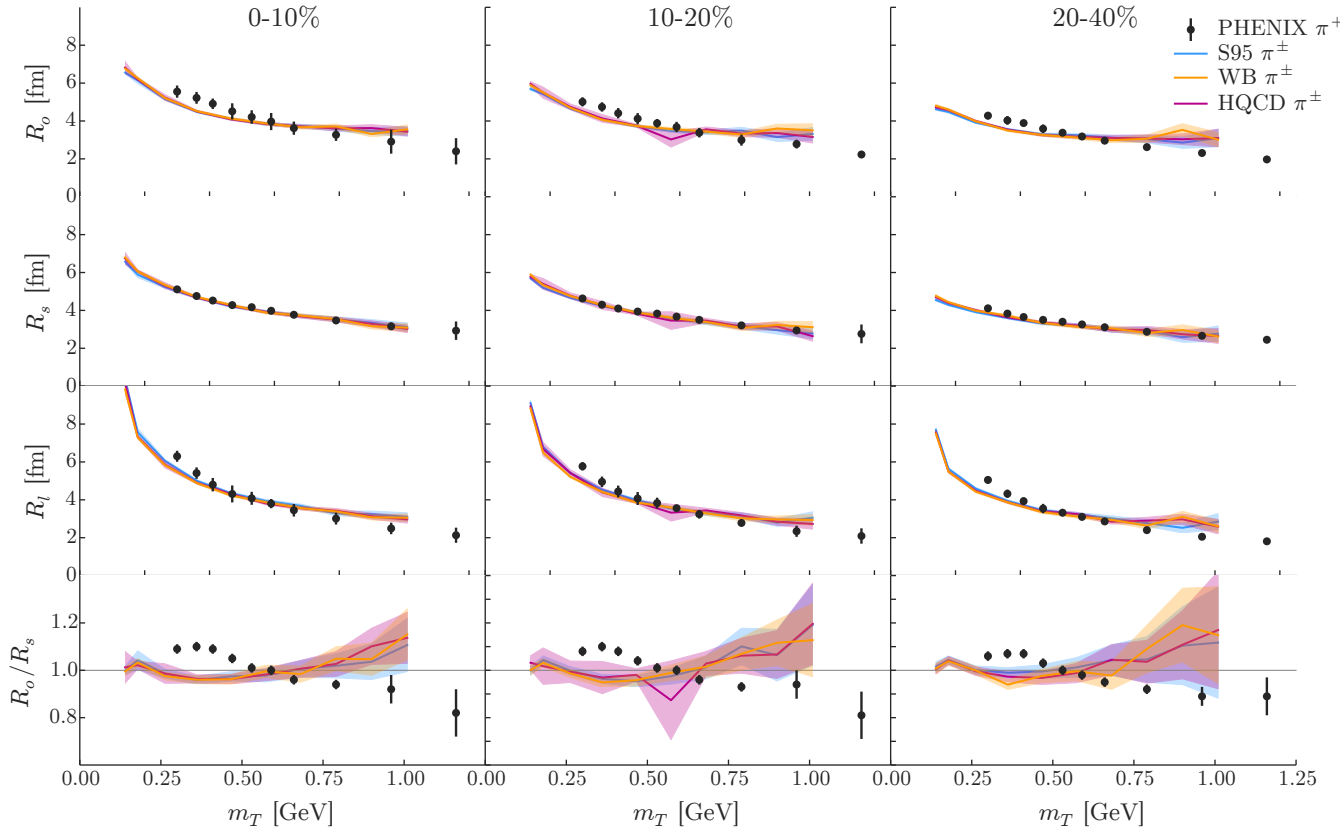


FIG. 7. Effect of the equation of state on the Bertsch-Pratt radii. We plot R_o , R_s , R_l and the ratio R_o/R_s (rows top to bottom) in centrality bins 0–10%, 20–30% and 40–50% (columns left to right) against transverse mass m_T for the HotQCD[†], WB[†] and S95[†] equations of state (purple, orange and blue lines). Shaded bands indicate two sigma errors estimated from the Jacobian of the fit function (21). Symbols with errors bars are experimental data from PHENIX.

of the three equations of state. Hence, the following results should be interpreted as a conservative *upper* bound on the goodness of fit sensitivity expected in a full hybrid model simulation.

Figs. 5 shows the elliptic flow v_2 of pions, kaons and protons calculated from equation (19) for the HotQCD[†], WB[†] and S95[†] equations of state in 0–10, 20–30 and 40–50% centrality bins. The first row of the figure shows the elliptic flow predicted by the HotQCD[†] equation of state while the middle and bottom rows display theoretical ratios of the WB[†] and S95[†] predictions over the HotQCD[†] result. The information in Fig. 6 is identical to that in Fig. 5 except that elliptic flow v_2 has been replaced with triangular flow v_3 .

We see in Fig. 5 that the elliptic flow generated by the HotQCD[†] and WB[†] parameterizations is in very good agreement across all centralities, while the S95[†] parameterization systematically generates $\sim 10\%$ less flow than the HotQCD[†] equation of state. This is consistent with previous findings that the S95[†] equation of state is considerably softer in the vicinity of the phase transition as evidenced by the speed of sound in Fig. 3.

In Fig. 6, we see that the effect on the triangular flow is similar to the effect observed on the elliptic flow

except more pronounced and generates as large as a 20% discrepancy in the peripheral flows predicted by the HotQCD[†] and S95[†] equations of state. This sensitivity of higher harmonics to the softness of the QGP phase equation of state puts the relatively large higher-order anisotropic flow coefficients observed at RHIC and the LHC into perspective.

C. Femtoscopic Bertsch-Pratt radii

The size of the fireball emission region is estimated using Hanbury-Brown-Twiss (HBT) interferometry for identical particles. The azimuthally averaged two-particle correlation function

$$C(q, k) = \frac{\sum_n \sum_{i,j} \delta_q \delta_k \Psi(q, r)}{\sum_n \sum_{i,j'} \delta_q \delta_k} \quad (20)$$

consists of a numerator with particles pairs sampled from the same event and a denominator with pairs sampled from different events. Here $q = p_i - p_j$ denotes the relative momentum, $r = x_i - x_j$ the relative separation

and $k = (p_i + p_j)/2$ the average momentum of the pion pair in the longitudinal co-moving frame where the component of k along the beam axis vanishes. The numerator is summed over all events n in a given centrality class and unique particle pair combinations i, j in each event. In the denominator, particle i is taken from one event and particle j' from a random partner event in the same centrality class. The delta functions δ_q and δ_k are 1 if the momenta q and k fall into their respective bins and 0 otherwise. Bose-Einstein correlations, which are not included natively in the UrQMD model, are imposed by adding the symmetrization factor $\Psi(q, r) = 1 + \cos q r$.

The average pair momentum k is then projected into its longitudinal component k_z and transverse component k_T , while the separation momentum q is represented in the orthogonal coordinates (q_o, q_s, q_l) , where q_l lies along the beam axis, q_o is parallel to k_T and q_s perpendicular to q_o and q_l . The resulting correlation function is approximated using a Gaussian source and fit to the parametric form

$$C(q_o, q_s, q_l, k_T) = \mathcal{N} \left(1 + \lambda e^{-R_o^2 q_o^2 - R_s^2 q_s^2 - R_l^2 q_l^2} \right) \quad (21)$$

by finding the best fit normalization \mathcal{N} , source strength λ and Bertsch-Pratt radii R_o , R_s and R_l for a given transverse momentum k_T .

We calculate the Bertsch-Pratt radii for each equation of state using identical pions. The fit is performed using $2 \cdot 10^4$ hydrodynamic events in each centrality bin and an additional ten UrQMD oversamples per event. The oversamples are then concatenated into a single particle list to increase the number of particle pairs by a factor 10^2 .

In Fig. 7, we plot the Bertsch-Pratt radii for the HotQCD[†], WB[†] and S95[†] equations of state as functions of the transverse mass $m_T = \sqrt{m^2 + k_T^2}$. The horizontal rows show the radii R_o , R_s , R_l and ratio R_o/R_s (top to bottom), while the columns mark centrality classes 0–10%, 10–20% and 20–40% (left to right). The different colored lines annotated in the legend indicate different equations of state and the bands estimate the error from the Jacobian of the fit. The symbols with error bars are experimental data from PHENIX.

We see that the Bertsch-Pratt radii predicted by the hybrid model provide a good description of the data across all centralities, except for at low p_T where R_o and R_l slightly undershoot the data. However, in contrast to spectra and flows we see no discernible difference in the Bertsch-Pratt radii predicted by the three different equations of state. This suggests that femptoscopic measurements are not sensitive enough to resolve small differences in the lattice equation of state.

D. HotQCD errors

In addition to the best fit parameterization shown in Fig. 1, the HotQCD analysis includes a detailed calculation of associated lattice errors. The errors enter the

analysis in several steps. The HotQCD trace anomaly is first calculated at various temperatures in the interval $130 < T < 400$ MeV using grids with temperal extent $N_\tau = 8, 10$ and 12 . For each temperature and grid size, the lattice simulation is repeated a large number of times. This creates a set of “data points” with a mean and variance determined from the Monte Carlo ensemble. Each data point is then resampled from its mean and variance, and the collection of resampled points, one for each value of the temperature T and grid size N_τ , is fit with the ansatz,

$$\frac{\theta^{\mu\mu}(T)}{T^4} = A + \sum_{i=1}^{n_k=3} B_i \times S_i(T) + \frac{C + \sum_{i=1}^{n_k=3} D_i \times S_i(T)}{N_\tau^2}. \quad (22)$$

Here the constants A , B_i , C and D_i are parameters of the fit, S_i is a set of cubic basis splines and n_k the number of knots used in the B-spline fitting. The entire procedure is then repeated 20,001 times to sample the function space of $\theta^{\mu\mu}(T)/T^4$ from the errors in the ensemble averaged lattice measurements.

In this section, we investigate the effect of the HotQCD lattice errors by measuring the spectra and flows for a subset of 100 randomly sampled splines determined according to equation (22). The piecewise interpolation procedure described in section II is applied to each spline to smoothly match the HotQCD lattice interaction measures with the HRG result at low temperature. The resulting interaction measures are shown in Fig. 8 along side the best fit HotQCD parameterization which naturally falls in the middle of the sampled curves. The vertical spread of the curves should be interpreted as the one sigma error band in the interval 180–400 MeV.

The energy density, entropy density, pressure and temperature are then calculated from each interaction measure according to (6) to generate 100 different EoS tables. Above 400 MeV, the higher derivatives of the interaction measures become unreliable and we extrapolate the EoS table using a simple power law. We note, however, that this modification has negligible impact on the hydrodynamic evolution at RHIC where the system is predomi-

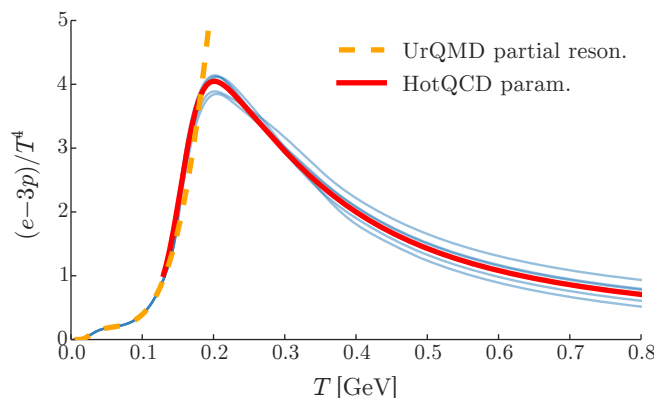


FIG. 8.

nantly below 400 MeV.

The HotQCD EoS samples are then used to repeat the spectra and flow analysis presented in section IV. We choose to omit Bertsch-Pratt radii due to the low sensitivity observed across the three different EoS and computational intensity required.

V. CONCLUSION AND OUTLOOK

ACKNOWLEDGMENTS

JSM acknowledges support by the DOE/NNSA Stockpile Stewardship Graduate Fellowship under grant no. DE-FC52-08NA28752.

-
- [1] P. Huovinen, Nucl. Phys. **A761**, 296 (2005), arXiv:nucl-th/0505036 [nucl-th].
 - [2] P. Huovinen and P. Petreczky, Nucl. Phys. **A837**, 26 (2010), arXiv:0912.2541 [hep-ph].
 - [3] S. Pratt, E. Sangaline, P. Sorensen, and H. Wang, Phys. Rev. Lett. **114**, 202301 (2015), arXiv:1501.04042 [nucl-th].
 - [4] S. Borsanyi, Z. Fodor, C. Hoelbling, S. D. Katz, S. Krieg, and K. K. Szabo, Phys. Lett. **B730**, 99 (2014), arXiv:1309.5258 [hep-lat].
 - [5] A. Bazavov *et al.* (HotQCD), Phys. Rev. **D90**, 094503 (2014), arXiv:1407.6387 [hep-lat].
 - [6] R. A. Soltz, C. DeTar, F. Karsch, S. Mukherjee, and P. Vranas, (2015), arXiv:1502.02296 [hep-lat].
 - [7] S. A. Bass *et al.*, Prog. Part. Nucl. Phys. **41**, 255 (1998), [Prog. Part. Nucl. Phys.41,225(1998)], arXiv:nucl-th/9803035 [nucl-th].
 - [8] M. Bleicher *et al.*, J. Phys. **G25**, 1859 (1999), arXiv:hep-ph/9909407 [hep-ph].
 - [9] A. Bazavov *et al.*, Phys. Rev. Lett. **113**, 072001 (2014), arXiv:1404.6511 [hep-lat].
 - [10] A. Adare *et al.* (PHENIX), (2015), arXiv:1506.07834 [nucl-ex].
 - [11] C. Shen, Z. Qiu, H. Song, J. Bernhard, S. Bass, and U. Heinz, (2014), arXiv:1409.8164 [nucl-th].
 - [12] C. Shen, *The standard model for relativistic heavy-ion collisions and electromagnetic tomography*, Ph.D. thesis, Ohio State University (2014).
 - [13] A. Adare *et al.* (PHENIX), Phys. Rev. **C78**, 044902 (2008), arXiv:0805.1521 [nucl-ex].
 - [14] A. Dumitru and Y. Nara, Phys. Rev. **C85**, 034907 (2012), arXiv:1201.6382 [nucl-th].
 - [15] J. S. Moreland, Z. Qiu, and U. W. Heinz, *Proceedings, 23rd International Conference on Ultrarelativistic Nucleus-Nucleus Collisions : Quark Matter 2012 (QM 2012)*, Nucl. Phys. **A904-905**, 815c (2013), arXiv:1210.5508 [nucl-th].
 - [16] P. Bozek and W. Broniowski, Phys. Rev. **C88**, 014903 (2013), arXiv:1304.3044 [nucl-th].
 - [17] R. E. Ansorge *et al.* (UA5), *In *Munich 1988, Proceedings, High energy physics* 647-648.*, Z. Phys. **C43**, 357 (1989).
 - [18] F. Karsch, D. Kharzeev, and K. Tuchin, Phys. Lett. **B663**, 217 (2008), arXiv:0711.0914 [hep-ph].